

This is an Open Access document downloaded from ORCA, Cardiff University's institutional repository: <https://orca.cardiff.ac.uk/id/eprint/163076/>

This is the author's version of a work that was submitted to / accepted for publication.

Citation for final published version:

Zhu, Jingxuan, Dai, Qiang, Xiao, Yuanyuan, Liu, Chaonan, Zhang, Jun, Zhuo, Lu and Han, Dawei 2023. Microphysics-based rainfall energy estimation using remote sensing and reanalysis data. *Journal of Hydrology* 627 (Part A) , 130314. 10.1016/j.jhydrol.2023.130314

Publishers page: <https://doi.org/10.1016/j.jhydrol.2023.130314>

Please note:

Changes made as a result of publishing processes such as copy-editing, formatting and page numbers may not be reflected in this version. For the definitive version of this publication, please refer to the published source. You are advised to consult the publisher's version if you wish to cite this paper.

This version is being made available in accordance with publisher policies. See <http://orca.cf.ac.uk/policies.html> for usage policies. Copyright and moral rights for publications made available in ORCA are retained by the copyright holders.



1 **Microphysics-based rainfall energy estimation using remote sensing and reanalysis data**

2 Jingxuan Zhu^{1,2,3}, Qiang Dai^{1,2,*}, Yuanyuan Xiao^{1,2}, Chaonan Liu^{1,2}, Jun Zhang^{1,2}, Lu Zhuo⁴, Dawei

3 Han³

4 ¹Key Laboratory of VGE of Ministry of Education, Nanjing Normal University, Nanjing, China

5 ²Jiangsu Center for Collaborative Innovation in Geographical Information Resource

6 Development and Application, Nanjing, China

7 ³Department of Civil Engineering, University of Bristol, Bristol, UK

8 ⁴School of Earth and Environmental Sciences, Cardiff University, Cardiff, UK

9 Corresponding author: Qiang Dai (qd_gis@163.com)

10

11 **1 Introduction**

12 In the context of global environmental challenges, such as climate change, land
13 degradation, and biodiversity loss, knowledge of soil erosion is more critical than ever before.
14 Soil erosion can have severe economic, environmental, and social impacts, including reduced
15 agricultural productivity, increased sedimentation of waterways, and reduced water quality.
16 Therefore, accurate measurement and prediction of soil erosion rates are essential for
17 identifying areas of high risk and developing appropriate mitigation measures. As is a driving
18 force of soil erosion, rainfall can significantly affect soil erosion rates by detaching and
19 transporting soil particles (Wischmeier and Smith, 1958). The erosive potential of rainfall on
20 soil, referred to as rainfall erosivity, is a key factor in soil erosion models, such as the Universal
21 Soil Loss Equation (USLE (Wischmeier and Smith, 1978)) and the Revised Universal Soil Loss
22 Equation (RUSLE (Renard, 1997)).

23 Recent research has emphasized the importance of adopting a microphysical perspective
24 when studying rainfall erosivity, which takes into account the interaction mechanism between
25 raindrops and soil. This interaction is primarily driven by the kinetic energy carried by
26 raindrops. Raindrops, with their impact force and energy, have the potential to cause soil
27 disintegration and mobilization. The size distribution of raindrops (DSD) is a critical factor that
28 affects their terminal fall velocity and kinetic energy, which ultimately determine the rainfall
29 erosivity. Disdrometers are devices used to measure the size and velocity of raindrops by using
30 laser or impact sensors. They are considered to be the most accurate method for measuring
31 DSD and have largely replaced older methods such as the paper and pellet method (Marshall
32 and Palmer, 1948; Wischmeier and Smith, 1958) or high-speed cameras (Jones, 1959; Kinnell,
33 1981; McIsaac, 1990).

34 However, due to the high cost of disdrometers, they cannot be widely deployed, and many

35 studies have instead used the empirical relationship to estimate rainfall energy. Previous studies
36 have relied on more easily accessible rainfall intensity records to estimate rainfall kinetic
37 energy (KE) using the empirical relationship between unit kinetic energy (KE) and intensity
38 (I). The exponential relationship between drop size and intensity was first observed by
39 (Marshall and Palmer, 1948), and since then, various forms of KE–I mathematical expressions
40 have been proposed for specific locations and climatic conditions, including power-law
41 (Meshesha et al., 2016; Park et al., 1980), linear (Nyssen et al., 2005; Sempere-Torres et al.,
42 1998), polynomial (Carter et al., 1974), logarithmic (Davison et al., 2005; Meshesha et al.,
43 2014; Wischmeier and Smith, 1958), and exponential (Brown and Foster, 1987; Kinnell, 1981;
44 Rosewell, 1986) relationships. Currently, the exponential function is preferentially used (Fornis
45 et al., 2005; Lim et al., 2015; Petan et al., 2010; Sanchez-Moreno et al., 2012; van Dijk et al.,
46 2002) due to its finite positive value at zero intensity and the asymptotic value at higher
47 intensities (Brown and Foster, 1987; Kinnell, 1976). Accurate KE–I relationships are derived
48 using DSD measured by disdrometers (Angulo-Martínez et al., 2016; Meshesha et al., 2016).
49 The most widely used KE–I relationship at present is recommended in the Revised Universal
50 Soil Loss Equation version 2 (RUSLE2) manual (USDA-Agricultural Research Service, 2013),
51 which is an exponential relationship between KE and rainfall intensity. This equation has been
52 widely adopted and used in various rainfall erosivity and soil erosion studies due to its
53 simplicity and ease of use (Fenta et al., 2023; Nearing et al., 2017; Panagos et al., 2017, 2015;
54 Xie et al., 2016).

55 Due to the limited availability of disdrometers, soil erosion estimation on a large scale
56 requires the use of satellite and reanalysis datasets, which are currently the mainstream and
57 future trends for obtaining precipitation information with high spatio-temporal resolution over
58 large areas. Compared to rain gauges and weather radars, satellite-based precipitation estimates
59 have significant advantages in terms of spatial coverage. They provide homogeneous

60 observation data, avoiding the high cost associated with ground observation networks, although
61 they may have longer revisiting periods (Hong et al., 2019). Since the launch of the Tropical
62 Rainfall Measuring Mission (TRMM) (Kummerow et al., 1998) in late 1997, various multi-
63 satellite precipitation products have emerged, such as the TRMM Multi-satellite Precipitation
64 Analysis (TMPA) (Huffman et al., 2007), Climate Prediction Center MORPHing technique
65 (CMORPH) (Joyce et al., 2004), and the Integrated Multi-satellitE Retrievals for Global
66 Precipitation Measurement (IMERG) (Huffman et al., 2020). Reanalysis precipitation products
67 (RPDs) provide long-term, spatially consistent and temporally continuous precipitation
68 estimates derived from numerical weather prediction models, assimilating diverse
69 observational data (Li et al., 2022). While RPDs are valuable for hydrological and ecological
70 modeling, as well as climate analyses, their accuracy is influenced by model physics and can
71 be sensitive to small changes in temperature and humidity fields (Li et al., 2022; Sharifi et al.,
72 2019). Additionally, they offer snowfall estimates that enable the evaluation of snowfall
73 estimates from satellite products (Tang et al., 2020). In recent years, significant advancements
74 have been made in data assimilation and model physics in reanalysis datasets. Commonly used
75 reanalysis datasets include ERA-Interim (Dee et al., 2011), ERA5 (Hersbach et al., 2020), and
76 ERA5-land (Muñoz Sabater, 2019) produced by the Medium-Range Weather Forecasts
77 (ECMWF), as well as Japanese 55-year Reanalysis 55-year Reanalysis (JRA-55) (Kobayashi
78 et al., 2015) by Japan Meteorological Agency (JMA) and Modern-Era Retrospective Analysis
79 for Research and Applications, version 2 (MERRA2) (Gelaro et al., 2017) by National
80 Aeronautics and Space Administration (NASA).

81 Currently, there are still two major knowledge gaps regarding the rainfall energy
82 estimation at a large-scale. Firstly, it is necessary to investigate the applicability of KE-I
83 relationships derived from disdrometer measurements in large-scale gridded precipitation data.
84 Disdrometers provide point-scale precipitation characteristics, and it is uncertain which KE-I

85 relationship derived from them can accurately be applied to those grid products. It is essential
86 to assess the compatibility of these relationships with remote sensing and reanalysis datasets to
87 ensure accurate and reliable estimation of rainfall energy at grid scales. Secondly, the
88 traditional approach of rainfall energy estimation on large-scale grids using the fixed KE–I
89 relationship introduces significant uncertainties as it neglects the spatial variability of the KE–
90 I relationship. By relying on fixed relationships, the spatial variations in rainfall characteristics
91 are disregarded. To address this issue, it is essential to incorporate the limited data from
92 disdrometers and explore spatially varying KE–I relationships. Such an approach can capture
93 the spatial variability of rainfall characteristics and provide more accurate estimations of
94 rainfall energy on the large scale.

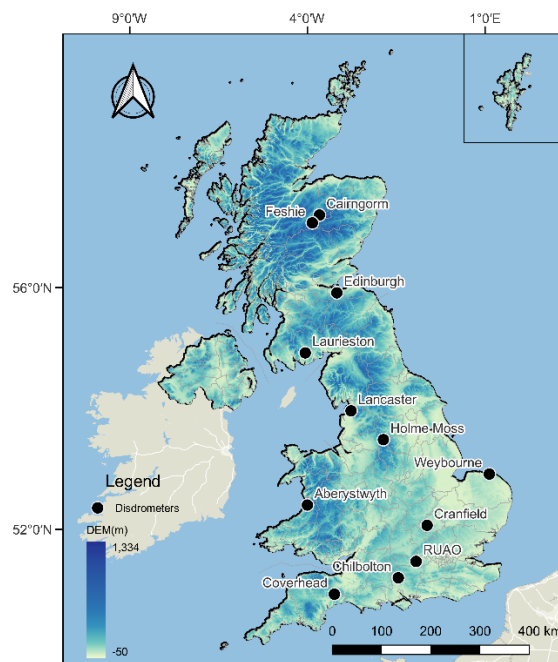
95 In our recent study, Dai et al. (2023) calculated global rainfall energy based on the
96 assumption that IMERG rainfall is accurate, using the DPR-based and RUSLE2-recommended
97 empirical formula. On this basis, this study aims to further compare the performance of fixed
98 (recommended in RUSLE2) and disdrometer-derived local microphysics-based KE–I
99 empirical relationships for estimating rainfall energy by using remote sensing satellite and
100 reanalysis precipitation datasets. The comparison is conducted across daily and monthly scales
101 to provide a comprehensive understanding of the differences between the methods. The results
102 of this study are expected to provide valuable insights into the applicability of using gridded
103 precipitation datasets for large-scale soil erosion estimation, as well as underscore the
104 significance of taking into account the unique characteristics of rainfall erosivity in different
105 regions.

106 **2 Study area and data**

107 **2.1 Study area**

108 This study focuses on the entire UK as the research area, investigating its rainfall erosivity

109 conditions. The UK is known for its varied climate conditions, with a temperate maritime
110 climate prevailing across most regions. The country experiences moderate to high rainfall
111 throughout the year, with the western regions receiving higher annual precipitation compared
112 to the eastern parts. Water is widely acknowledged as the primary driver of soil erosion in the
113 United Kingdom, with a greater emphasis placed on water erosion compared to wind erosion
114 (Evans et al., 2017). This focus is mainly attributed to the vulnerability of arable land, where
115 the soil is exposed and susceptible to erosion during the annual cycle of sowing and subsequent
116 harvesting. According to the government report, the utilized agricultural area in the UK is of
117 substantial extent, covering approximately 16.8 million hectares in 2022, which accounts for a
118 significant 69% of the country's total land area. The exposure of bare cultivated land increases
119 the risk of erosion caused by rainfall and runoff. Evans et al. (2017) assessed the risk of soil
120 erosion by water in England and Wales, revealing that areas with a moderate or higher level of
121 risk are widespread across the whole England. Panago et al. (2021) predicted that soil erosion
122 in the UK will increase by approximately 20% to 50% compared to the levels estimated in 2016
123 by the year 2050.



124

125 **Figure 1** DEM map with disdrometer distribution in the study area.

126 **2.2 Data**

127 **2.2.1 Ground DSD data**

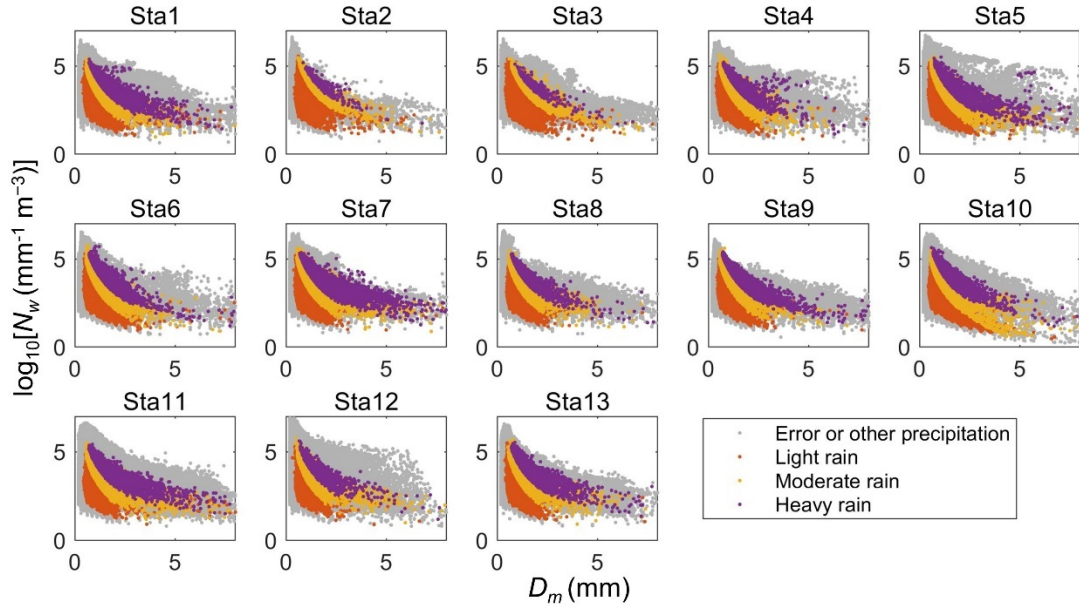
128 Disdrometer Verification Network (DiVeN) (Pickering et al., 2019) served as the reference
129 for measuring drop size distribution (DSD) in this study. The network consisted of 14 Thies
130 Clima Laser Precipitation Monitor (LPM) disdrometers deployed across the entire UK from
131 2017 to 2019. It is worth noting that, for the purpose of this investigation, data from 13 LPMs
132 were used due to the absence of spectrum data from the 14th disdrometer located at Coverhead.
133 Unfortunately, one of the disdrometers located at Coverhead did not provide DSD data,
134 resulting in the utilization of 13 LPMs for the investigation (Figure 1). Each LPM has a
135 measuring horizontal area of 45.6 cm², with dimensions of 228 mm in length, 20 mm in width,
136 and 0.75 mm in thickness. The LPM employs a method of measuring the maximum attenuation
137 of the signal to determine the size of precipitation particles. Additionally, it estimates the fall
138 velocity of these particles by analyzing the duration of their presence within the laser beam.
139 Equipped with this technology, an LPM is capable of recording the number of raindrops passing
140 through 22 unequal diameter bins ranging from 0.125 to 8 mm, as well as 20 unequal velocity
141 bins ranging from 0 to 10 m·s⁻¹, every minute. Further details regarding the specific data
142 availability for each disdrometer can be found in Table 1.

143 **Table 1** Information of 13 available LPMs in DiVeN.

ID	Name	Latitude (°)	Longitude (°)	Start date	End date	Number of available records
1	Chilbolton	51.15	-1.44	2017/2/10	2019/9/30	59,019
2	Chilbolton2	51.15	-1.44	2017/2/10	2018/3/12	25,265
3	RUAO	51.44	-0.94	2017/2/13	2019/9/30	59,576

4	Cranfield	52.07	-0.63	2017/2/16	2019/8/23	55,396
5	Weybourne	52.95	1.12	2017/2/17	2019/9/30	56,787
6	Aberystwyth	52.42	-4	2017/2/20	2019/9/30	82,060
7	Lancaster	54.01	-2.77	2017/2/22	2019/9/30	66,450
8	Edinburgh	55.92	-3.17	2017/2/24	2019/9/30	55,960
9	Laurieston	54.96	-4.06	2017/4/21	2019/9/30	86,642
10	Holme Moss	53.53	-1.86	2017/3/10	2019/9/30	52,105
11	Cairngorm	57.13	-3.66	2017/6/14	2019/9/30	64,093
12	Feshie	57.01	-3.86	2017/6/14	2019/9/30	18,210
13	Coverhead	50.86	-3.24	2017/11/8	2019/9/30	42,755

144 Disdrometers are used to study the microphysical processes of rainfall and has the ability
145 to divide precipitation types, such as drizzle, rain, snow, grains and hail, as recorded in present
146 weather (PW) code (Pickering et al., 2019). In this study, LPM recorded the diameter and fall
147 velocity of all observed raindrops into 22 and 20 bins in the 1-minute interval. After processing
148 data quality control referring to Yang et al. (2022), data points with rainfall intensities below
149 $0.1 \text{ mm}\cdot\text{h}^{-1}$ (Dai et al., 2020; Yang et al., 2019; Zhu et al., 2021) and those identified as non-
150 rain records by the present weather code were also excluded to eliminate interference. Figure
151 2 illustrates the scatter plot of the mass weighted mean drop diameter (D_m) and normalised
152 intercept parameter (N_w) relationship before and after the filtering process based on the
153 disdrometer. The colored dots represent PW code-defined different types of rainfall (light,
154 moderate and heavy) considered in this study, while the gray dots represent errors or other types
155 of precipitation that were not taken into account in this analysis. Taking the Chilbolton1 site as
156 an example, where the number of data records in minute resolution was reduced from 353,006
157 to 59,019. The number of available records for each station is displayed in Table 1.



158

159 **Figure 2.** Scatter plot of $\log_{10}N_w-D_m$ for different precipitation types at 13 disdrometer stations.
 160 Note: Colored dots represent different precipitation levels defined by PW codes considered in
 161 this study, where orange represents light rain, yellow represents moderate rain, purple
 162 represents heavy rain, and gray represents errors or other precipitation types excluded from the
 163 analysis.

164 **2.2.2 IMERG dataset**

165 Among multi-satellite precipitation products, IMERG is considered one of the most
 166 reliable satellite-based rainfall estimation datasets. It utilizes the combined precipitation
 167 estimates from various satellite passive microwave (PMW) sensors in the Global Precipitation
 168 Measurement (GPM) constellation using the Goddard Profiling Algorithm (GPROF2017)
 169 (Randel et al., 2020). The estimates are intercalibrated to the GPM Combined Ku Radar-
 170 Radiometer Algorithm (CORRA) product and merged into half-hourly $0.1^\circ \times 0.1^\circ$ fields
 171 (Huffman et al., 2020). For this study, the Final Run of the GPM Level 3 product IMERG V06
 172 was used to represent remote sensing observations at a resolution of $0.1^\circ \times 0.1^\circ$ and a temporal
 173 resolution of 30 minutes within $60^\circ\text{S}-60^\circ\text{N}$, which is calibrated using vertically integrated
 174 vapor from MERRA2 and Global Precipitation Climatology Centre monthly gauges. In

175 addition, Mahmoud et al. (2021) evaluated the performance of IMERG in Finland (60°-70°N)
176 and found that more than 60% of rainfall events were detected even in the 60°-63°N range. In
177 general, it has a latency of about 3.5 months, and the precipitationCal field, which represents
178 the fully calibrated precipitation, is the most appropriate data field for research purposes
179 (Huffman et al., 2020).

180 **2.2.3 ERA5-land precipitation dataset**

181 ERA5-land (Muñoz Sabater, 2019), also known as the fifth-generation global reanalysis
182 dataset for land, is the latest global land reanalysis from ECMWF, represents a notable
183 advancement in terms of spatiotemporal resolutions compared to its predecessors, ERA-
184 Interim (Dee et al., 2011) and ERA5 (Hersbach et al., 2020). It offers high-resolution and
185 quality-controlled data specifically tailored for land surface applications. With a spatial
186 resolution of 0.1° (~9 km), ERA5-land provides detailed information on various meteorological
187 variables such as temperature, precipitation, wind, and radiation, covering the entire globe.
188 ERA5-land has a comprehensive temporal coverage starting from 1950 to 2-3 months before
189 the present day, allowing researchers and practitioners to analyze long-term trends and
190 variability in land surface conditions. It is a replay of the land component of the ERA5 climate
191 reanalysis, forced by meteorological fields from ERA5. Notably, ERA5-land always uses
192 forcing fields based on the final release of ERA5 (Muñoz Sabater, 2019). ERA5-land comes
193 with a series of improvements that enhance its accuracy for all types of land applications. It
194 incorporates advancements in land surface models and assimilates a wide range of
195 observational data, including satellite observations, ground-based measurements, and
196 reanalysis data. These enhancements result in more reliable estimates of meteorological
197 variables at the land surface, making ERA5-land a valuable resource for climate research, water
198 resource management, ecosystem modeling, and weather forecasting at regional and global
199 scales.

200 3 Methodology

201 3.1 DSD model

202 The variability of the DSD model is typically represented using a normalized three-
203 parameter gamma model (Dai et al., 2020; Dai and Han, 2014; Ulbrich, 1983), which is
204 expressed as follows:

$$N(D) = N_w f(\mu) \left(\frac{D}{D_m}\right)^\mu \exp\left[-\frac{(4+\mu)D}{D_m}\right], \quad (1)$$

205 where $N(D)$ represents the number of particles comprised by each unit diameter interval, D_m
206 (mm) is the mass-weighted mean drop diameter parameter of the gamma DSD, N_w ($\text{mm}^{-1}\cdot\text{m}^{-3}$)
207 is the normalised intercept parameter, $\Gamma(n)$ is the mathematical gamma function, and $f(\mu)$ is a
208 function of the shape parameter μ , which is defined as:

$$f(\mu) = \frac{6(4+\mu)^{\mu+4}}{4^4 \Gamma(\mu+4)}. \quad (2)$$

209 Therefore, $N(D)$ using disdrometer records can be calculated by summing up the number
210 of raindrops in each diameter and velocity range, as shown below:

$$N(D_i) = \sum_{i=1, j=1}^{I, J} \frac{n_{i,j}}{A \Delta t v_j \Delta D_i} \quad (3)$$

211 where I and J represent diameter and velocity bin numbers respectively, D_i (mm) denotes the
212 mean volume equivalent diameter of the i th size class, v_j ($\text{m}\cdot\text{s}^{-1}$) is the mean particle speed for
213 velocity class j , n_{ij} is the number of raindrops at the specific diameter bin i and velocity bin j ,
214 A_i (m^2) is the sampling area of sensor, and Δt and ΔD are the sampling range of time and
215 diameter, respectively.

216 3.2 Rainfall energy estimation

217 Rainfall energy is a critical parameter in soil erosion research as it governs the detachment,
218 transportation, and deposition of soil particles. It is defined as the energy carried by the
219 raindrops in motion and is determined by the size and velocity of the individual raindrops. The
220 mathematical expression for the kinetic energy of a raindrop (e , unit: J) can be written as
221 follows:

$$e = \frac{1}{2}mv^2 = \frac{1}{12}10^{-6}\pi\rho v_i^2 D_i^3 \quad (4)$$

222 where ρ is the water density ($1 \text{ g}\cdot\text{cm}^{-3}$). The total kinetic energy of raindrops falling in the
223 unit volume, or KE ($\text{J}\cdot\text{m}^{-2}\cdot\text{mm}^{-1}$), is generally used to express rainfall energy. The KE of the
224 t th time step (KE_t) can be calculated as follows:

$$KE_t = \frac{e_t}{Ap_t} = \frac{1}{Ap_t} \sum_{i=1}^{I,J} n_{i,j} e_{i,j} \quad (5)$$

225 where e_t (J) and p_t (mm) are the total raindrop kinetic energy and rainfall depth during t th time
226 step. As the disdrometer has a sampling interval of 1 minute, equation (5) can be rewritten as:

$$KE_t = \frac{e_t}{AI_t} = \frac{60}{AI_t} \sum_{i=1}^{I,J} n_{i,j} e_{i,j} \quad (6)$$

$$I_t = 6\pi \times 10^{-4} \int N(D)D^3V(D)dD \quad (7)$$

227 where I_t is the rainfall intensity ($\text{mm}\cdot\text{h}^{-1}$) calculated from the DSD data during the t th minute.

228 Thus, on the daily scale, the daily rainfall energy (E_d) represents the sum of the storm
229 energy over all time steps in a day, which is calculated as follows:

$$E_d = \sum_{t=1}^T \frac{KE_t I_t}{60} \quad (8)$$

230 where $T=1440$ is the number of minutes in a whole day.

231 **3.3 Development of KE–I relationship models**

232 In regions where disdrometers are not available, rainfall KE_t can be estimated using
 233 empirical relationships based on rainfall intensity (I) using mathematical forms. In order to
 234 investigate more accurate estimations of large-scale rainfall energy, this study formulated four
 235 models for generating KE-I relationships, all of which were expressed in an exponential form,
 236 expressed as:

$$KE = e_{\max} [1 - a \exp(-bI)] \quad (9)$$

237 where e_{\max} is the average maximum value of energy measured under high rainfall intensity, and
 238 a and b are coefficients that model the curve of the equation.

239 The first model, F1, represented the fixed KE–I relationship recommended by USDA-
 240 Agricultural Research Service (2013) for RUSLE2. It assigns a value of 29 to e_{\max} , with
 241 coefficients a set at 0.72 and b at 0.082, and incorporates an improved b based on the research
 242 by Brown and Foster (1987). This empirical function has been extensively adopted and applied
 243 in various regions across the globe (Nearing et al., 2017; Panagos et al., 2017, 2015; Xie et al.,
 244 2016). The second model, F2, utilized a partially fitted curve that incorporated disdrometer
 245 data while maintaining a fixed e_{\max} value of 29. The coefficients a and b were derived from
 246 fitting the disdrometer data. To constrain the equation, an assumption was made regarding the
 247 value of e_{\max} , following the recommendations of Rosewell (1986) and Brown and Foster (1987).
 248 In the third model, F3, e_{\max} was set to the mean KE value corresponding to high precipitation
 249 intensity ($>40 \text{ mm}\cdot\text{h}^{-1}$) before other coefficients were fitted. This model recognizes that e_{\max}

250 may vary regionally, implying that different locations may exhibit regional differences in KE
 251 values. Finally, the fourth model, F4, was a fully fitted curve in which all three coefficients
 252 (e_{max} , a, and b) were derived from fitting the disdrometer data. In this model, e_{max} was treated
 253 as a coefficient without a specific physical interpretation, and its value was determined purely
 254 to optimize the equation fitting.

255 3.4 Evaluation methods

256 Five metrics, including Pearson correlation coefficient (CC), mean absolute error (MAE),
 257 mean bias error (MBE), root mean square error (RMSE), relative bias (BIAS) and standard
 258 deviation (STD), were selected to evaluate the accuracy and error of using the fixed and
 259 disdrometer-derived local microphysics-based KE–I relationships in the IMERG and ERA5
 260 products to calculate rainfall erosivity against dense disdrometers. CC describes the strength
 261 of association between the rainfall energy of large-scale datasets and ground observations.
 262 MAE quantifies the average magnitude of errors, while MBE shows whether the average error
 263 is positive or negative. RMSE measures the standard deviation of the errors. BIAS represents
 264 the difference between the estimated and observed values, normalized by the mean of observed
 265 values. These metrics mentioned above are defined in Table 2.

266 **Table 2.** Statistical evaluation metrics for evaluating the rainfall erosivity estimation ability of
 267 grid products.

Evaluation Metrics	Formulas	Perfect value
Spearman correlation coefficient (CC)	$CC = \frac{\sum (E_i - \bar{E})(O_i - \bar{O})}{\sqrt{\sum (E_i - \bar{E})^2} \sqrt{\sum (O_i - \bar{O})^2}}$	1
Mean absolute error (MAE)	$MAE = \frac{\sum O_i - E_i }{n}$	0

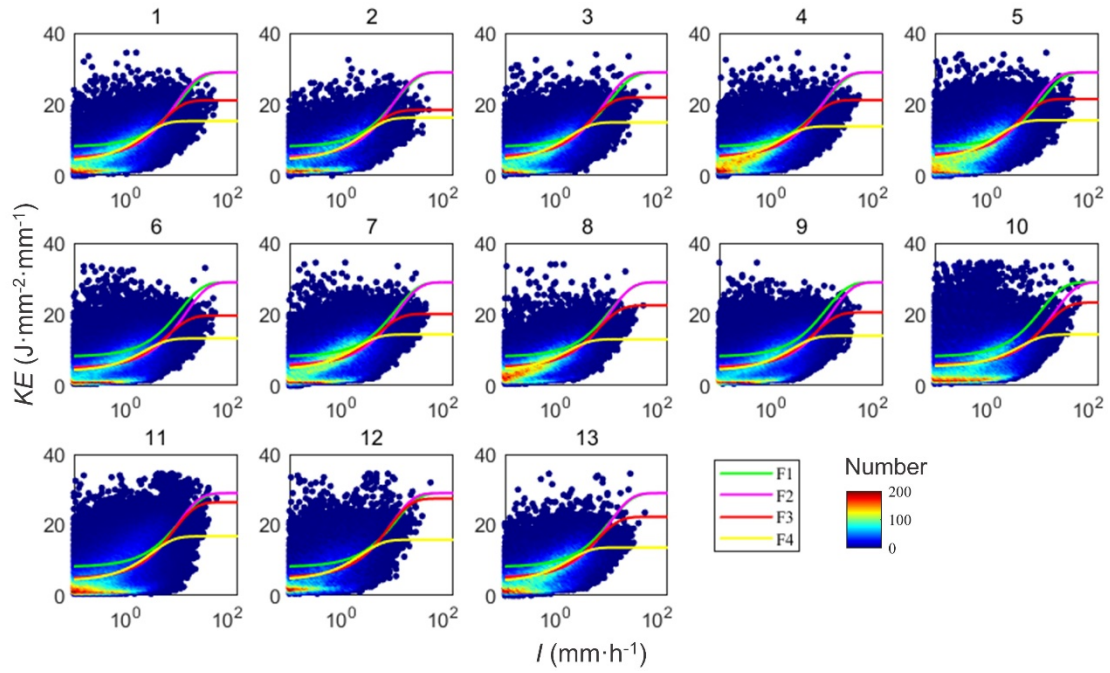
Mean bias error (MBE)	$MBE = \frac{\sum(O_i - E_i)}{n}$	0
Root mean square error (RMSE)	$RMSE = \sqrt{\frac{1}{n} \sum(O_i - E_i)^2}$	0
Relative bias (BIAS)	$BIAS = \frac{\sum(E_i - O_i)}{\sum O_i} \times 100\%$	0%
Standard deviation (STD)	$STD = \sqrt{\frac{1}{N} \sum(E_i - \bar{E})^2}$	0

268 where n is the number of samples. E_i and O_i are the values of the valuated data from grid
 269 products and observed data from ground disdrometers, respectively, for the i th sample. \bar{E}
 270 and \bar{O} are the mean values of E_i and O_i , respectively.

271 4 Results

272 4.1 Disdrometer-derived KE–I relationships

273 Figure 3 shows the occurrences of KE–I relationships together with fitting curves derived
 274 by the four models (F1 to F4), calculated from the disdrometer data at 13 different sites. Table
 275 3 presents the coefficients associated with each curve for every site. The results reveal that the
 276 majority of KE–I records are concentrated in the range of low KE ($<15 \text{ J}\cdot\text{m}^{-2}\cdot\text{mm}^{-1}$) and low I
 277 ($<10 \text{ mm}\cdot\text{h}^{-1}$) values. Combined with the curves, we found that the challenge faced by F1 model
 278 in capturing the geographical variability of rainfall microphysical characteristics. The e_{\max}
 279 value in F1 often exceeds the actual values observed at these stations. In contrast, F4, as a fully
 280 fitted model, aligns well with the dense range of KE–I data as expected. However, its KE
 281 plateau value is frequently lower, leading to an underestimation of kinetic energy for high-
 282 intensity raindrops.



283

284 **Figure 3.** Occurrences of KE–I with fitting curves generated from the four models on 13
 285 disdrometer stations.

286 **Table 3.** Coefficients of different KE–I models on 13 disdrometer stations.

ID	F1			F2			F3			F4		
	e_{max}	a	b	e_{max}	a	b	e_{max}	a	b	e_{max}	a	b
1	29	0.72	0.082	29	0.82	0.101	21.11	0.78	0.197	15.31	0.74	0.437
2	29	0.72	0.082	29	0.82	0.094	18.42	0.75	0.246	16.24	0.73	0.333
3	29	0.72	0.082	29	0.81	0.108	21.95	0.77	0.199	14.95	0.71	0.531
4	29	0.72	0.082	29	0.81	0.094	21.2	0.76	0.185	13.84	0.69	0.575
5	29	0.72	0.082	29	0.80	0.112	21.54	0.75	0.22	15.57	0.71	0.534
6	29	0.72	0.082	29	0.82	0.066	19.65	0.76	0.146	13.23	0.69	0.398
7	29	0.72	0.082	29	0.80	0.079	20.11	0.73	0.183	14.34	0.68	0.48
8	29	0.72	0.082	29	0.82	0.088	22.5	0.77	0.142	13.01	0.67	0.564

9	29	0.72	0.082	29	0.82	0.066	20.55	0.76	0.134	13.97	0.70	0.368
10	29	0.72	0.082	29	0.80	0.046	23.29	0.75	0.069	14.34	0.63	0.211
11	29	0.72	0.082	29	0.83	0.095	26.42	0.82	0.113	16.77	0.75	0.296
12	29	0.72	0.082	29	0.82	0.103	27.46	0.81	0.114	15.8	0.72	0.394
13	29	0.72	0.082	29	0.82	0.09	22.29	0.78	0.152	13.61	0.71	0.54

287 Table 4 shows the CC values obtained by comparing the F1 to F4 models with the
288 measured data from the disdrometer networks at each station. The results indicate that F4
289 exhibits the best CC performance, which represents the fully fitted curve, followed closely by
290 F3. The fixed coefficient model F1 and fixed- e_{\max} model F2 shows the similar worst correlation
291 effect. These results suggest that the fully fitted model (F4) can capture the dense distribution
292 of KE-I values even though some KE values at high rainfall intensity may be underestimated.
293 The partial fitting models (F3), which take into account the local maximum KE value at high
294 rainfall intensity, also provide a good representation of the KE-I relationship at individual sites.
295 In contrast, relationship models with fixed parameters are retained, including fully fixed (F1)
296 and partially fixed (F2) are not appropriate for all sites in the UK, especially generate higher
297 KE with high rainfall intensity.

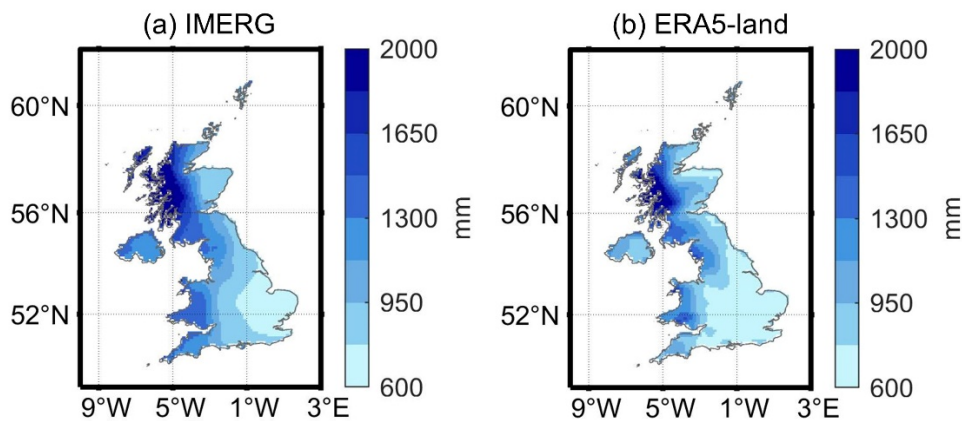
298 **Table 4.** CC of different KE-I models on 13 disdrometer stations.

Station ID	F1	F2	F3	F4
1	0.59	0.59	0.62	0.63
2	0.56	0.56	0.59	0.59
3	0.56	0.57	0.59	0.61
4	0.54	0.54	0.57	0.59
5	0.55	0.56	0.59	0.60
6	0.50	0.49	0.52	0.53

7	0.53	0.53	0.56	0.57
8	0.54	0.54	0.56	0.58
9	0.54	0.54	0.56	0.57
10	0.39	0.38	0.39	0.40
11	0.49	0.49	0.49	0.50
12	0.48	0.49	0.49	0.51
13	0.55	0.56	0.57	0.60

299 **4.2 Rainfall energy estimation based on the conventional fixed KE–I relationship.**

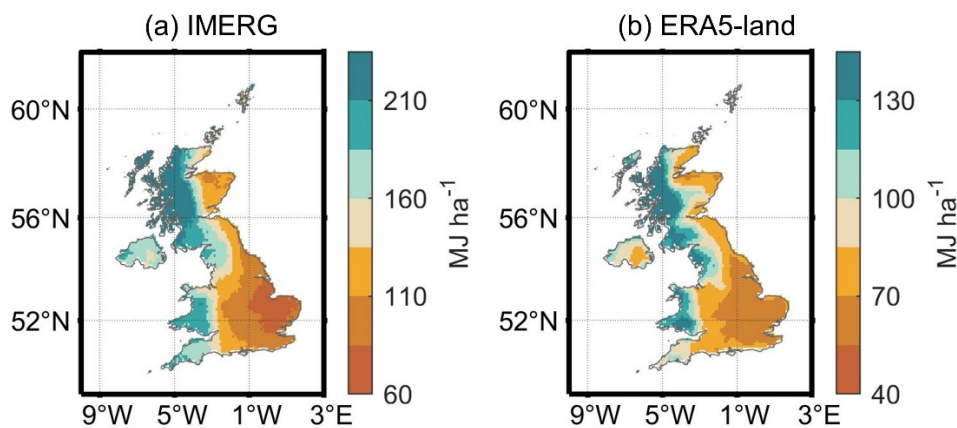
300 To align with the 1-hour resolution of ERA5-land, the 30-minute rainfall intervals within
301 the IMERG dataset were aggregated into corresponding 1-hour intervals. In conventional
302 methods for estimating rainfall energy, F1 is commonly used as a fixed KE–I empirical
303 equation. Figure 4 illustrates the gridded annual cumulative rain in the UK in 2018, based on
304 IMERG and ERA5-land datasets at a spatial resolution of 0.1°. In Figures 4(a) and 4(b), the
305 spatial distribution of rainfall in both large-scale precipitation datasets exhibit similar patterns.
306 Under the influence of prevailing westerly winds, high annual rainfall values are concentrated
307 in the mountainous regions of northwestern UK, gradually decreasing from west to east.
308 Overall, IMERG shows higher annual rain compared to ERA5-land, although the highest
309 regional annual rain is a little higher in ERA5-land (2486.2 mm) than in IMERG (2336.9 mm).



310

311 **Figure 4.** Spatial distribution of annual cumulative rain (mm) in 2018 across the whole UK.

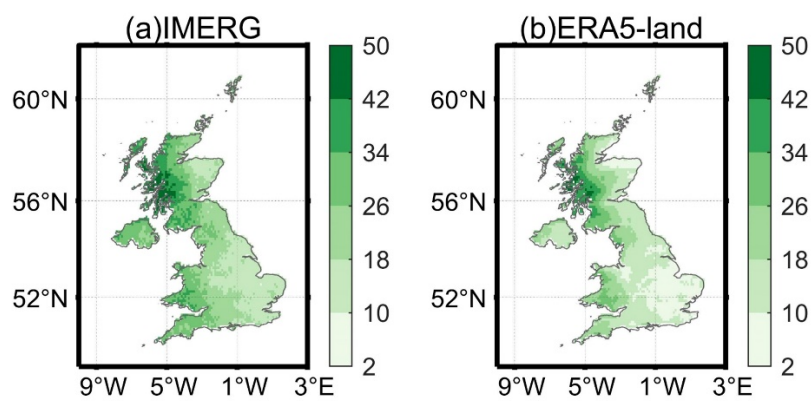
312 Based on rainfall grid data, Figure 5 illustrates the spatial distribution of annual cumulative
313 rainfall energy in the UK in 2018 calculated using the widely used KE–I model F1. When
314 comparing these results with the spatial distribution of rainfall depicted using the same data
315 source shown in Figure 4, we observe a general similarity in the corresponding regions. This
316 implies that regions with higher precipitation values tend to exhibit higher rainfall energy
317 values. However, while the spatial distribution of cumulative rainfall energy obtained from
318 IMERG and ERA5-land exhibits similarities, there are significant differences in their
319 magnitudes. The annual energy values calculated from IMERG are nearly twice as large as
320 those obtained from ERA5-land.



321
322 **Figure 5.** Spatial distribution of annual cumulative rainfall energy in 2018 across the whole
323 UK.

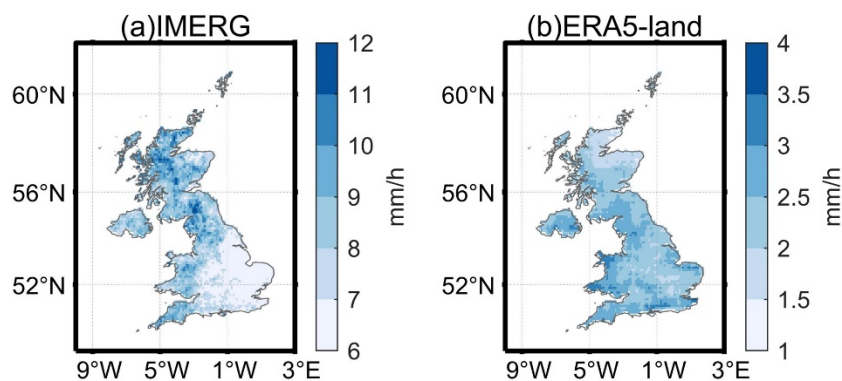
324 To investigate the reasons for the notable differences using the two data sources in rainfall
325 energy, we compared the number of erosive rainfall events and the maximum rainfall intensity
326 at the grid level. Figure 6 and 7 presents the number and maximum intensity maps of erosive
327 rainfall events in the UK throughout the year 2018, as calculated by IMERG and ERA5-land.
328 The rainfall time series was divided into rainfall events by separating them into consecutive 6-
329 hour dry periods (Dai et al., 2020). Subsequently, erosive rainfall events were classified based

330 on the criteria proposed by Wischmeier and Smith (1958), which consider continuous rainfall
 331 events with a total precipitation exceeding 12.7 mm as erosive. In addition, the maximum 30-
 332 minute rainfall intensity (I_{30}) of erosive rainfall events is an important factor in calculating
 333 rainfall erosivity. In rainfall products with hourly intervals, I_{30} is often approximated by
 334 multiplying the maximum rainfall intensity by a conversion constant (Yin et al., 2007).
 335 Therefore, in this study, the hourly maximum rainfall intensity (I_m) is used to represent the
 336 characteristics of I_{30} .



337

338 **Figure 6.** Number of erosive rainfall events in 2018, estimated by IMERG and ERA5-land.



339

340 **Figure 7.** Mean I_m of erosive rainfall events in 2018, estimated by IMERG and ERA5-land.

341 From Figure 6, it can be observed that, in nearly all grids, IMERG identifies slightly more
 342 erosive events compared to ERA5-land. This observation is related to the differences in total
 343 annual rainfall between the two datasets shown in Figure 4(a) and 4(b). Similarly, the number

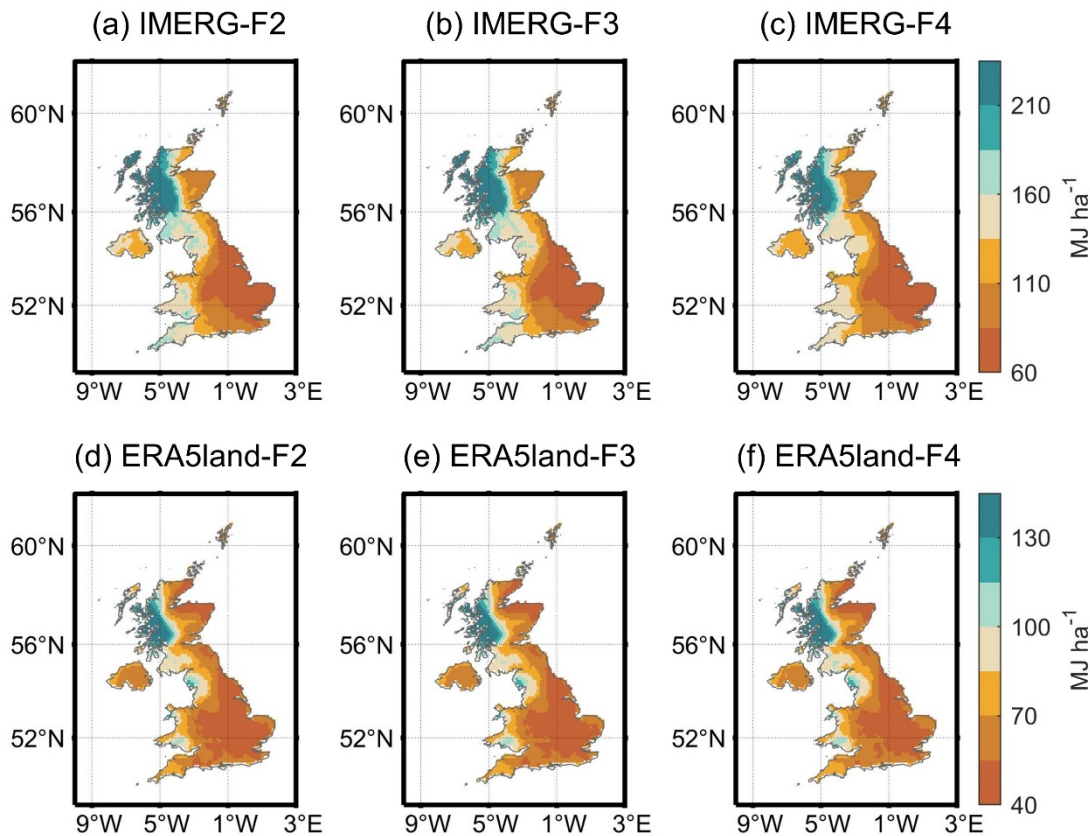
344 of erosive rainfall events decreases from west to east. In 2018, IMERG identifies fewer erosive
345 events than ERA5-land in only 135 grid cells (~4% of the total study area), and in 70% of the
346 grid cells, the number of IMERG-identified erosive events exceed 30% of corresponding
347 ERA5-land events. Furthermore, IMERG identifies over 50% of the erosion events in 49% of
348 the grid cells in comparison with ERA5-land.

349 Figures 7 represent the average I_m values of the erosive rainfall events in 2018. It can be
350 observed that IMERG generally exhibits higher I_m values, with values consistently above 5
351 $\text{mm}\cdot\text{h}^{-1}$. Approximately 7.68% of the grid cells have an average I_m exceeding $10 \text{ mm}\cdot\text{h}^{-1}$, and
352 the trend shows a decreasing pattern from north to south. In contrast, ERA5-land results (Figure
353 5d) show higher average I_m values in the southern coastal areas of the UK, while inland regions
354 of England and northern Scotland have extremely low I_m values. Nearly no grid cells in the
355 entire UK exceed $3.5 \text{ mm}\cdot\text{h}^{-1}$ in the ERA5-land estimates. It is worth noting that the IMERG
356 product represents the snapshot of rainfall intensity observed by microwave sensors, whereas
357 ERA5-land data represents hourly accumulated rainfall obtained from reanalysis. Therefore,
358 the different methods of rainfall acquisition may significantly affect the calculation of I_m and
359 subsequently impact the estimation of rainfall erosivity.

360 **4.3 Rainfall energy estimation based on the three microphysics-fitting KE-I** 361 **relationship.**

362 Figure 8 illustrates the estimates of rainfall energy in the UK using the fitted models (F2-
363 F4), which more or less consider local variations in rainfall microphysical characteristics. Each
364 grid cell utilizes the KE-I formula from the nearest station during the rainfall energy calculation
365 process (details are provided in Table 3). Specifically, Figures 8(a)-(c) depict the estimates
366 obtained by combining IMERG with the F2-F4 formulas, while Figures 8(d)-(f) show the
367 estimates obtained by combining ERA5-land data with the same three formulas. It is evident

368 that when the two kinds of large-scale rainfall product are combined with the F2-F4 formulas,
 369 the overall estimates of rainfall energy are lower compared to the results obtained using the F1
 370 formula in Figure 5. This is particularly noticeable in the notable reduction of rainfall energy
 371 values in western regions of England and Wales, as well as the expanded range of low energy
 372 values in eastern England.



373
 374 **Figure 8.** Spatial distribution of E using the three microphysics-fitting KE–I relationship.

375 For the calculations using IMERG (Figures 8a-c), the E values obtained from the fully
 376 fitted KE–I formula (F4) are consistently the lowest. In the case of the Northern Ireland region,
 377 the E area with values in the range of 110-135 MJ·ha⁻¹ is the largest, while only a few grids
 378 exceed 135 MJ·ha⁻¹ of E. In particular, in Figure 8(c), there are almost no areas in Wales that
 379 exceed 160 MJ·ha⁻¹ of E, whereas sporadic grid cells surpass this threshold in Figures 8(a) and
 380 8(b). However, for the IMERG-based E estimates using F1, the majority of areas in Wales have
 381 E values greater than 160 MJ·ha⁻¹, indicating a substantial impact of the use of different KE–I

382 formulas on the calculation of rainfall energy. On the other hand, for the ERA5-land results
 383 (Figures 8d-f), the differences in E values obtained using the three fitting formulas (F2-F4) are
 384 relatively small.

385 **4.4 Evaluation of KE–I relationships and accumulated rainfall energy evaluation**
 386 **using disdrometer data**

387 Table 5 presents the CC between the KE values calculated using different empirical
 388 relationships from IMERG and ERA5-land datasets, and the mean KE values derived from
 389 disdrometer data at the corresponding rainfall intensities for each site. In Table 5, almost all
 390 CC values exceed 0.90, and the results exhibit a similar pattern to Table 4, where the overall
 391 correlation is higher for ERA5-land compared to IMERG results. It is worth noting that the
 392 higher CC values in Fig. 5 are mainly due to the averaging of the disdrometer results for each
 393 rainfall intensity. Additionally, both IMERG and ERA5-land estimations show the highest CC
 394 values when using the fully fitted formula F4. For IMERG, the majority of CC values for F4
 395 exceed 0.95, while for ERA5-land, most CC values for F4 even surpass 0.98, significantly
 396 outperforming the corresponding CC values for F1, which are around 0.90 and 0.95,
 397 respectively. The strong correlation with the mean KE values from the disdrometer indicates
 398 the rationality and feasibility of utilizing the KE–I relationship for rainfall energy estimation
 399 using both large-scale remote sensing precipitation products and reanalysis datasets.

400 **Table 5.** CC of different KE–I models between estimated KE and disdrometer-derived mean
 401 KE in the same rain value in each station.

Station ID	IMERG				ERA5-land			
	F1	F2	F3	F4	F1	F2	F3	F4
1	0.92	0.93	0.96	0.98	0.97	0.97	0.98	0.99

2	0.92	0.93	0.95	0.96	0.95	0.95	0.97	0.97
3	0.92	0.93	0.96	0.98	0.96	0.97	0.97	0.99
4	0.90	0.91	0.94	0.98	0.95	0.95	0.96	0.99
5	0.91	0.92	0.95	0.98	0.96	0.96	0.97	0.99
6	0.93	0.93	0.95	0.98	0.95	0.95	0.96	0.98
7	0.91	0.91	0.95	0.98	0.95	0.95	0.96	0.98
8	0.91	0.92	0.93	0.96	0.95	0.95	0.96	0.99
9	0.94	0.94	0.96	0.99	0.96	0.96	0.96	0.98
10	0.92	0.91	0.92	0.95	0.91	0.90	0.91	0.92
11	0.94	0.94	0.95	0.97	0.97	0.97	0.97	0.98
12	0.89	0.90	0.90	0.92	0.93	0.93	0.93	0.95
13	0.90	0.91	0.93	0.97	0.96	0.96	0.97	0.99

402 Table 6 presents the averaged indicators (excluding outliers, defined as data points falling
403 below the lower quartile minus 1.5 times the interquartile range or above the upper quartile
404 plus 1.5 times the interquartile range) for the evaluation of daily E results calculated from
405 IMERG and ERA5-land at 13 stations. It can be observed that for daily E computed from
406 IMERG, the results obtained using the F4 relationship perform the best. They exhibit the
407 highest correlation (0.63) with daily E derived from the disdrometer data. Additionally, the
408 deviation from the IMERG-derived E is the smallest (98.22 MJ·ha⁻¹) for the F4 relationship.
409 At the same time, the ERA5-land daily E values calculated using the four KE–I relationships
410 show a higher correlation with the disdrometer results, with mean values around 0.66 for all
411 stations. Interestingly, for ERA5-land, the F1 formula yields the best MBE and BIAS, with
412 BIAS even approaching zero (-1.11%). This is because the F1 evaluation of ERA5-land’s daily
413 E shows notable variation between stations, resulting in a median MBE and BIAS close to zero,
414 as the high positive and negative values tend to offset each other. In summary, for daily E, CC

415 values of ERA5-land are higher than those of IMERG, and the F4 model consistently
 416 demonstrates the best overall performance across different data sources

417 **Table 6.** Station-averaged indicators for evaluating daily E.

Indicator	IMERG				ERA5-land			
	F1	F2	F3	F4	F1	F2	F3	F4
CC	0.607	0.605	0.590	0.630	0.664	0.660	0.660	0.662
MAE	51.97	47.25	47.89	43.84	33.98	33.06	33.10	32.99
MBE	-17.69	-8.04	-8.18	-4.80	3.68	14.56	14.94	13.78
RMSE	109.59	98.37	102.74	86.28	54.67	56.42	56.60	56.12
BIAS	48.85	28.77	29.02	21.37	1.11	-22.58	-23.46	-20.73
STD	126.78	111.84	115.87	98.22	52.21	42.91	41.54	44.75

418 Similarly, an evaluation of the monthly E calculated by IMERG and ERA5-land was also
 419 conducted (for months with complete disdrometer records), shown in Table 7. The results
 420 revealed that at the monthly scale, the CC values for the four formula options were very similar,
 421 with minimal differences among them, especially for the results of ERA5-land. However, when
 422 considering the error metrics, the F4 relationship consistently outperformed the other options.
 423 These findings imply that, regardless of the dataset (IMERG or ERA5-land) used for monthly
 424 E calculations, the selection of the formula does not significantly affect the correlation between
 425 the calculated values and the disdrometer data at the monthly scale. However, the F4 formula
 426 consistently offers the advantage of minimizing errors, thereby providing a more accurate
 427 estimation of monthly E. This highlights the importance of considering the appropriate formula
 428 when assessing erosive rainfall at longer time scales, as the F4 formula can provide reliable
 429 and robust results.

430 **Table 7.** Station-averaged indicators for evaluating monthly E.

Indicator	IMERG				ERA5-land			
	F1	F2	F3	F4	F1	F2	F3	F4
CC	0.655	0.651	0.640	0.673	0.685	0.687	0.686	0.688
MAE	568.73	467.83	473.23	427.43	332.06	327.91	329.22	326.59
MBE	-456.44	-280.96	-282.92	-227.36	-97.89	104.46	109.37	93.06
RMSE	703.05	594.86	605.30	543.92	387.37	372.36	374.14	370.69
BIAS	84.28	59.09	59.35	50.32	26.90	-3.79	-4.59	-1.88
STD	521.12	452.04	462.50	410.85	335.39	264.68	258.72	273.52

431 **5 Discussions**

432 This study utilizes large-scale radar remote sensing and reanalysis rainfall datasets to
433 investigate the impact of fixed and fitted KE–I relationships on rainfall energy calculation. The
434 KE–I formula is a commonly used method for estimating rainfall energy, but the conventional
435 fixed coefficient values neglect the spatial variations in rainfall microphysical characteristics.
436 Therefore, this study compared the performance of four kinds of KE–I relationships to estimate
437 site-specific rainfall energy and investigate the differences in the results across the UK. The
438 results reveal that in most cases, rainfall energy calculated using the conventional fixed KE–I
439 relationship tend to be notably higher than those calculated using the KE–I relationships that
440 considers rainfall microphysical characteristics. However, there are several key issues with the
441 estimation of rainfall erosivity using large-scale precipitation products:

442 Firstly, differences in rainfall acquisition methods between satellite observations and
443 reanalysis datasets lead to significant discrepancies in calculated rainfall erosivity, despite
444 similar total rainfall amounts. IMERG provides instantaneous rainfall intensity observed by
445 microwave sensors, while ERA5-land offers accumulated rainfall obtained from reanalysis. It
446 is important to note that in IMERG, it is usually assumed that the observed rainfall rate applies
447 for the entire half-hour period. In addition, to align with the 1-hour resolution of ERA5-land,

448 the 30-minute rainfall intervals in IMERG were aggregated into 1-hour intervals. However,
449 despite this adjustment, IMERG precipitation still exhibits extreme values, resulting in a high
450 positive bias. This suggests an overall overestimation of rainfall energy in IMERG, leading to
451 higher I_m values for erosive rainfall events. On the other hand, erosive rainfall events tend to
452 have higher I_m values in IMERG due to the presence of more high-intensity values. On the
453 other hand, ERA5-land rainfall data generates lower I_m values due to fewer high-intensity
454 values. This discrepancy leads to an underestimation of erosivity.

455 Secondly, ground validation of rainfall poses a challenge for large-scale rainfall products.
456 Grid-based data (in this study, 0.1° resolution) deviates from point-based observations. While
457 large-scale rainfall products perform well at daily/monthly scales, discrepancies become
458 apparent at finer hourly scales. Xu et al. (2019) found that the R-squared value between IMERG
459 (V04 and V05) and ground observation station rainfall intensity was only around 0.1 at the
460 hourly scale, while it improved to 0.44 and 0.50 at the daily scale for V04 and V05, respectively.
461 Moazami and Najafi (2021) discovered that in both the western and eastern coastal regions of
462 Canada, IMERG V06 tends to overestimate precipitation intensity by approximately 25%. The
463 differences between satellite-based data and ground-based observations are even more
464 pronounced for more intense rainfall events. Qin et al. (2021) compared hourly precipitation
465 from ERA5 and ground gauges in eastern China and found that ERA5 reproduces the spatial
466 patterns of precipitation climatology. However, it tends to overestimate the frequency of
467 rainfall events while underestimating their intensity. Additionally, the disdrometer itself
468 introduces measurement errors, data gaps, and other computational errors during the E
469 estimation process, making it difficult to obtain long-term and accurate rainfall energy
470 sequences. For instance, Fehlmann et al. (2020) conducted a study in Switzerland and
471 discovered that the LPM system consistently underestimated rainfall intensities by 16.5%.
472 Similarly, Guyot et al. (2019) observed that the LPM underestimated liquid precipitation and

473 the number of raindrops from 0.75 millimeters to larger diameters compared to OTT Parsivel¹.
474 Furthermore, the uptime of DiVeN is not complete all the time (Pickering et al., 2019), which
475 may result in lower calculated rainfall energy.

476 Finally, for subsequent estimates of rainfall erosivity estimation, the universal threshold of
477 12.7 mm for erosive rainfall events, proposed in the USLE (Universal Soil Loss Equation)
478 (Wischmeier and Smith, 1978), may not be applicable to all large-scale rainfall products due
479 to variations in rainfall characteristics. This threshold is derived from erosion observations in
480 US agricultural fields. Due to the different characteristics of large-scale rainfall products, it is
481 not necessarily suitable to use this threshold to define erosive rainfall events for each product.
482 Therefore, determining the erosive rainfall threshold specific to each rainfall product and even
483 the threshold for erosive rainfall energy requires further exploration in future research. These
484 challenges highlight the need for careful consideration and evaluation when using large-scale
485 rainfall products for rainfall erosivity calculations.

486 **6 Conclusions**

487 In conclusion, this study focused on the investigation of rainfall energy estimation and its
488 spatial distribution using different models of KE–I relationship. Two main issues were
489 addressed: 1) the suitability of KE–I relationships derived from disdrometer data for gridded
490 precipitation datasets, considering the regional variability in rainfall characteristics captured
491 by the disdrometer; and 2) the uncertainty introduced by using fixed KE–I relationships for
492 calculating large-scale grid-based rainfall energy, as these relationships neglect the spatial
493 variability of KE–I relationships and overlook the spatial variation of rainfall characteristics.
494 By addressing these issues, the study aimed to provide insights into improving the accuracy of
495 rainfall energy estimation at larger scales. Several key findings have emerged from this
496 investigation:

- 497 1. Conventional methods for estimating rainfall erosivity using fixed KE–I relationships
498 do not account for regional differences in rainfall microphysical characteristics. In the
499 context of the UK, this approach tends to overestimate KE values for high rainfall
500 intensities.
- 501 2. Fitting coefficients to the KE–I relationship improve the correlation of the estimations.
502 Among the fitted formulas, F4, which is a total fitting relationship of KE–I, exhibits the
503 highest CC, followed by F3 with a local e_{\max} value.
- 504 3. IMERG and ERA5-land yield comparable annual rainfall totals across the entire UK,
505 with similar spatial distribution patterns. However, there are significant differences in
506 the results for rainfall energy, with annual rainfall energy values calculated from
507 IMERG being almost twice as high as those calculated from ERA5-land. In addition,
508 IMERG found more than 50% more erosive events than ERA5-land in almost half of
509 the grid cells.
- 510 4. The high values of annual rainfall energy in the UK are concentrated in the mountainous
511 regions of the northwest, gradually decreasing from west to east. Of the estimated
512 rainfall energy values, those estimated using the conventional fixed KE–I relationship
513 (F1) tend to have the highest values, while those using the full-fitting relationship (F4)
514 have the smallest energy values.
- 515 5. ERA5-land demonstrates stronger correlation and lower error in estimating rainfall
516 energy compared to IMERG. However, it tends to underestimate rainfall intensity
517 overall.

518 These findings underscore the importance of considering regional rainfall microphysical
519 characteristics and employing fitted KE–I relationships for more accurate estimations of
520 rainfall erosivity. Additionally, they highlight the significant differences in rainfall energy

521 results obtained from different datasets, emphasizing the need for careful interpretation and
522 selection of appropriate rainfall datasets when assessing erosion potential. Further research
523 should focus on refining KE–I relationships, determining regional representation of
524 disdrometer-derived formulas and exploring the impact of various rainfall acquisition methods
525 on erosivity estimations to enhance erosion risk assessments and inform erosion control
526 strategies.

527

528 **Acknowledgments**

529 This study was supported by the National Natural Science Foundation of China (Nos.
530 41871299 and 42201020).

531 **References**

- 532 1. Angulo-Martínez, M., Beguería, S., Kysely, J., 2016. Use of disdrometer data to evaluate the
533 relationship of rainfall kinetic energy and intensity (KE-I). *Sci. Total Environ.* 568, 83–94.
534 <https://doi.org/10.1016/j.scitotenv.2016.05.223>
- 535 2. Brown, L.C., Foster, G.R., 1987. Storm erosivity using idealized intensity distributions. *Trans. ASAE*
536 30, 379–386.
- 537 3. Carter, C.E., Greer, J.D., Braud, H.J., Floyd, J.M., 1974. Raindrop Characteristics in South Central
538 United States. *Trans. ASAE* 17, 1033–1037.
- 539 4. Dai, Q., Han, D., 2014. Exploration of discrepancy between radar and gauge rainfall estimates driven
540 by wind fields. *Water Resour. Res.* 50, 8571–8588. <https://doi.org/10.1002/2014WR015794>
- 541 5. Dai, Q., Zhu, J., Lv, G., Kalin, L., Yao, Y., Zhang, J., & Han, D. (2023). Radar remote sensing reveals
542 potential underestimation of rainfall erosivity at the global scale. *Sci. Adv.* 9(32), eadg5551.

543 <https://doi.org/10.1126/sciadv.adg5551>

544 6. Dai, Q., Zhu, J., Zhang, S., Zhu, S., Han, D., Lv, G., 2020. Estimation of rainfall erosivity based on
545 WRF-derived raindrop size distributions. *Hydrol. Earth Syst. Sci.* 24, 5407–5422.
546 <https://doi.org/10.5194/hess-24-5407-2020>

547 7. Davison, P., Hutchins, M.G., Anthony, S.G., Betson, M., Johnson, C., Lord, E.I., 2005. The relationship
548 between potentially erosive storm energy and daily rainfall quantity in England and Wales. *Sci. Total
549 Environ., Linking Landscape Sources of Phosphorus and Sediment to Ecological Impacts in Surface
550 Waters* 344, 15–25. <https://doi.org/10.1016/j.scitotenv.2005.02.002>

551 8. Dee, D.P., Uppala, S.M., Simmons, A.J., Berrisford, P., Poli, P., Kobayashi, S., Andrae, U., Balmaseda,
552 M.A., Balsamo, G., Bauer, P., Bechtold, P., Beljaars, A.C.M., van de Berg, L., Bidlot, J., Bormann, N.,
553 Delsol, C., Dragani, R., Fuentes, M., Geer, A.J., Haimberger, L., Healy, S.B., Hersbach, H., Hólm, E.V.,
554 Isaksen, L., Kållberg, P., Köhler, M., Matricardi, M., McNally, A.P., Monge-Sanz, B.M., Morcrette, J.-
555 J., Park, B.-K., Peubey, C., de Rosnay, P., Tavolato, C., Thépaut, J.-N., Vitart, F., 2011. The ERA-
556 Interim reanalysis: configuration and performance of the data assimilation system. *Q. J. R. Meteorol.
557 Soc.* 137, 553–597. <https://doi.org/10.1002/qj.828>

558 9. Evans, R., Collins, A.L., Zhang, Y., Foster, I.D.L., Boardman, J., Sint, H., Lee, M.R.F., Griffith, B.A.,
559 2017. A comparison of conventional and ¹³⁷Cs-based estimates of soil erosion rates on arable and
560 grassland across lowland England and Wales. *Earth-Sci. Rev.* 173, 49–64.
561 <https://doi.org/10.1016/j.earscirev.2017.08.005>

562 10. Fehlmann, M., Rohrer, M., von Lerber, A., Stoffel, M., 2020. Automated precipitation monitoring with
563 the Thies disdrometer: biases and ways for improvement. *Atmospheric Meas. Tech.* 13, 4683–4698.
564 <https://doi.org/10.5194/amt-13-4683-2020>

- 565 11. Fenta, A. A., Tsunekawa, A., Haregeweyn, N., Yasuda, H., Tsubo, M., Borrelli, P., Kawai, T., Belay, A.
566 S., Ebabu, K., Berihun, M, L., Sultan, D, Setargie, T. A., Elnashar, A., Panagos, P. (2023). Improving
567 satellite-based global rainfall erosivity estimates through merging with gauge data. *J. Hydrol.* 620,
568 129555. <https://doi.org/10.1016/j.jhydrol.2023.129555>
- 569 12. Fornis, R.L., Vermeulen, H.R., Nieuwenhuis, J.D., 2005. Kinetic energy–rainfall intensity relationship
570 for Central Cebu, Philippines for soil erosion studies. *J. Hydrol.* 300, 20–32.
571 <https://doi.org/10.1016/j.jhydrol.2004.04.027>
- 572 13. Gelaro, R., McCarty, W., Suárez, M.J., Todling, R., Molod, A., Takacs, L., Randles, C.A., Darmenov,
573 A., Bosilovich, M.G., Reichle, R., Wargan, K., Coy, L., Cullather, R., Draper, C., Akella, S., Buchard,
574 V., Conaty, A., Silva, A.M. da, Gu, W., Kim, G.-K., Koster, R., Lucchesi, R., Merkova, D., Nielsen,
575 J.E., Partyka, G., Pawson, S., Putman, W., Rienecker, M., Schubert, S.D., Sienkiewicz, M., Zhao, B.,
576 2017. The Modern-Era Retrospective Analysis for Research and Applications, Version 2 (MERRA-2).
577 *J. Clim.* 30, 5419–5454. <https://doi.org/10.1175/JCLI-D-16-0758.1>
- 578 14. Guyot, A., Pudashine, J., Protat, A., Uijlenhoet, R., Pauwels, V.R.N., Seed, A., Walker, J.P., 2019. Effect
579 of disdrometer type on rain drop size distribution characterisation: a new dataset for south-eastern
580 Australia. *Hydrol. Earth Syst. Sci.* 23, 4737–4761. <https://doi.org/10.5194/hess-23-4737-2019>
- 581 15. Hersbach, H., Bell, B., Berrisford, P., Hirahara, S., Horányi, A., Muñoz-Sabater, J., Nicolas, J., Peubey,
582 C., Radu, R., Schepers, D., Simmons, A., Soci, C., Abdalla, S., Abellan, X., Balsamo, G., Bechtold, P.,
583 Biavati, G., Bidlot, J., Bonavita, M., De Chiara, G., Dahlgren, P., Dee, D., Diamantakis, M., Dragani,
584 R., Flemming, J., Forbes, R., Fuentes, M., Geer, A., Haimberger, L., Healy, S., Hogan, R.J., Hólm, E.,
585 Janisková, M., Keeley, S., Laloyaux, P., Lopez, P., Lupu, C., Radnoti, G., de Rosnay, P., Rozum, I.,
586 Vamborg, F., Villaume, S., Thépaut, J.-N., 2020. The ERA5 global reanalysis. *Q. J. R. Meteorol. Soc.*

- 587 146, 1999–2049. <https://doi.org/10.1002/qj.3803>
- 588 16. Hong, Y., Tang, G., Ma, Y., Huang, Q., Han, Z., Zeng, Z., Yang, Y., Wang, C., Guo, X., 2019. Remote
589 Sensing Precipitation: Sensors, Retrievals, Validations, and Applications. pp. 107–128.
590 https://doi.org/10.1007/978-3-662-48297-1_4
- 591 17. Huffman, G.J., Bolvin, D.T., Braithwaite, D., Hsu, K., Joyce, R., Kidd, C., Nelkin, E.J., Sorooshian, S.,
592 Tan, J., Xie, P., 2020. NASA Global Precipitation Measurement (GPM) Integrated Multi-satellitE
593 Retrievals for GPM (IMERG).
- 594 18. Huffman, G.J., Bolvin, D.T., Nelkin, E.J., Wolff, D.B., Adler, R.F., Gu, G., Hong, Y., Bowman, K.P.,
595 Stocker, E.F., 2007. The TRMM Multisatellite Precipitation Analysis (TMPA): Quasi-Global, Multiyear,
596 Combined-Sensor Precipitation Estimates at Fine Scales. *J. Hydrometeorol.* 8, 38–55.
597 <https://doi.org/10.1175/JHM560.1>
- 598 19. Ji, L., Chen, H., Li, L., Chen, B., Xiao, X., Chen, M., Zhang, G., 2019. Raindrop Size Distributions and
599 Rain Characteristics Observed by a PARSIVEL Disdrometer in Beijing, Northern China. *Remote Sens.*
600 11, 1479. <https://doi.org/10.3390/rs11121479>
- 601 20. Jones, D.M.A., 1959. THE SHAPE OF RAINDROPS. *J. Atmospheric Sci.* 16, 504–510.
602 [https://doi.org/10.1175/1520-0469\(1959\)016<0504:TSOR>2.0.CO;2](https://doi.org/10.1175/1520-0469(1959)016<0504:TSOR>2.0.CO;2)
- 603 21. Joyce, R.J., Janowiak, J.E., Arkin, P.A., Xie, P., 2004. CMORPH: A Method that Produces Global
604 Precipitation Estimates from Passive Microwave and Infrared Data at High Spatial and Temporal
605 Resolution. *J. Hydrometeorol.* 5, 487–503. [https://doi.org/10.1175/1525-7541\(2004\)005<0487:CAMTPG>2.0.CO;2](https://doi.org/10.1175/1525-7541(2004)005<0487:CAMTPG>2.0.CO;2)
- 606
- 607 22. Kinnell, P. i. a., 1981. Rainfall Intensity-Kinetic Energy Relationships for Soil Loss Prediction. *Soil*
608 *Sci. Soc. Am. J.* 45, 153–155. <https://doi.org/10.2136/sssaj1981.03615995004500010033x>

- 609 23. Kinnell, P.I.A., 1976. Some Observations on the Joss-Waldvogel Rainfall Disdrometer. *J. Appl.*
610 *Meteorol.* 1962-1982 15, 499–502.
- 611 24. Kobayashi, S., Ota, Y., Harada, Y., Ebata, A., Moriya, M., Onoda, H., Onogi, K., Kamahori, H.,
612 Kobayashi, C., Endo, H., Miyaoka, K., Takahashi, K., 2015. The JRA-55 Reanalysis: General
613 Specifications and Basic Characteristics. *J. Meteorol. Soc. Jpn. Ser II* 93, 5–48.
614 <https://doi.org/10.2151/jmsj.2015-001>
- 615 25. Kummerow, C., Barnes, W., Kozu, T., Shiue, J., Simpson, J., 1998. The Tropical Rainfall Measuring
616 Mission (TRMM) Sensor Package. *J. Atmospheric Ocean. Technol.* 15, 809–817.
617 [https://doi.org/10.1175/1520-0426\(1998\)015<0809:TTRMMT>2.0.CO;2](https://doi.org/10.1175/1520-0426(1998)015<0809:TTRMMT>2.0.CO;2)
- 618 26. Li, X., Qin, X., Yang, J., Zhang, Y., 2022. Evaluation of ERA5, ERA-Interim, JRA55 and MERRA2
619 reanalysis precipitation datasets over the Poyang Lake Basin in China. *Int. J. Climatol.* 42, 10435–
620 10450. <https://doi.org/10.1002/joc.7915>
- 621 27. Lim, Y.S., Kim, J.K., Kim, J.W., Park, B.I., Kim, M.S., 2015. Analysis of the relationship between the
622 kinetic energy and intensity of rainfall in Daejeon, Korea. *Quat. Int., Quaternary Studies in Korea III:*
623 *Contents and characteristics of paleoclimatology/paleoceanography studies in and around Korea* 384,
624 107–117. <https://doi.org/10.1016/j.quaint.2015.03.021>
- 625 28. Mahmoud, M. T., Mohammed, S. A., Hamouda, M. A., Dal Maso, M., Mohamed, M. M. (2021).
626 Performance of the IMERG precipitation products over high-latitudes region of Finland. *Remote Sens.*
627 13(11), 2073.
- 628 29. Marshall, J.S., Palmer, W.M.K., 1948. THE DISTRIBUTION OF RAINDROPS WITH SIZE. *J.*
629 *Atmospheric Sci.* 5, 165–166. [https://doi.org/10.1175/1520-](https://doi.org/10.1175/1520-0469(1948)005<0165:TDORWS>2.0.CO;2)
630 [0469\(1948\)005<0165:TDORWS>2.0.CO;2](https://doi.org/10.1175/1520-0469(1948)005<0165:TDORWS>2.0.CO;2)

- 631 30. McIsaac, G.F., 1990. Apparent geographic and atmospheric influences on raindrop sizes and rainfall
632 kinetic energy. *J. Soil Water Conserv.* 45, 663–666.
- 633 31. Meshesha, D.T., Tsunekawa, A., Tsubo, M., Haregeweyn, N., Adgo, E., 2014. Drop size distribution
634 and kinetic energy load of rainfall events in the highlands of the Central Rift Valley, Ethiopia. *Hydrol.*
635 *Sci. J.* 59, 2203–2215. <https://doi.org/10.1080/02626667.2013.865030>
- 636 32. Meshesha, D.T., Tsunekawa, A., Tsubo, M., Haregeweyn, N., Tegegne, F., 2016. Evaluation of kinetic
637 energy and erosivity potential of simulated rainfall using Laser Precipitation Monitor. *CATENA* 137,
638 237–243. <https://doi.org/10.1016/j.catena.2015.09.017>
- 639 33. Moazami, S., Najafi, M.R., 2021. A comprehensive evaluation of GPM-IMERG V06 and MRMS with
640 hourly ground-based precipitation observations across Canada. *J. Hydrol.* 594, 125929.
641 <https://doi.org/10.1016/j.jhydrol.2020.125929>
- 642 34. Muñoz Sabater, J., 2019. ERA5-Land hourly data from 1950 to present.
643 <https://doi.org/10.24381/cds.e2161bac>
- 644 35. Nearing, M.A., Yin, S., Borrelli, P., Polyakov, V.O., 2017. Rainfall erosivity: An historical review.
645 *CATENA* 157, 357–362. <https://doi.org/10.1016/j.catena.2017.06.004>
- 646 36. Nyssen, J., Vandenreyken, H., Poesen, J., Moeyersons, J., Deckers, J., Haile, M., Salles, C., Govers, G.,
647 2005. Rainfall erosivity and variability in the Northern Ethiopian Highlands. *J. Hydrol.* 311, 172–187.
648 <https://doi.org/10.1016/j.jhydrol.2004.12.016>
- 649 37. Panagos, P., Ballabio, C., Borrelli, P., Meusburger, K., Klik, A., Rousseva, S., Tadić, M.P., Michaelides,
650 S., Hrabalíková, M., Olsen, P., Aalto, J., Lakatos, M., Rymaszewicz, A., Dumitrescu, A., Beguería, S.,
651 Alewell, C., 2015. Rainfall erosivity in Europe. *Sci. Total Environ.* 511, 801–814.
652 <https://doi.org/10.1016/j.scitotenv.2015.01.008>

- 653 38. Panagos, P., Ballabio, C., Himics, M., Scarpa, S., Matthews, F., Bogonos, M., Poesen, J., Borrelli, P.,
654 2021. Projections of soil loss by water erosion in Europe by 2050. *Environ. Sci. Policy* 124, 380–392.
655 <https://doi.org/10.1016/j.envsci.2021.07.012>
- 656 39. Panagos, P., Borrelli, P., Meusburger, K., Yu, B., Klik, A., Jae Lim, K., Yang, J.E., Ni, J., Miao, C.,
657 Chattopadhyay, N., Sadeghi, S.H., Hazbavi, Z., Zabihi, M., Larionov, G.A., Krasnov, S.F., Gorobets,
658 A.V., Levi, Y., Erpul, G., Birkel, C., Hoyos, N., Naipal, V., Oliveira, P.T.S., Bonilla, C.A., Meddi, M.,
659 Nel, W., Al Dashti, H., Boni, M., Diodato, N., Van Oost, K., Nearing, M., Ballabio, C., 2017. Global
660 rainfall erosivity assessment based on high-temporal resolution rainfall records. *Sci. Rep.* 7, 4175.
661 <https://doi.org/10.1038/s41598-017-04282-8>
- 662 40. Park, S.W., Mitchell, J.K., Bubenzer, G.D., 1980. Splash erosion modeling: physical analyses. *Trans.*
663 *ASAE* 25, 357–361.
- 664 41. Petan, S., Rusjan, S., Vidmar, A., Mikoš, M., 2010. The Rainfall Kinetic Energy–Intensity Relationship
665 for Rainfall Erosivity Estimation in the Mediterranean Part of Slovenia. *J. Hydrol.* 391, 314–321.
666 <https://doi.org/10.1016/j.jhydrol.2010.07.031>
- 667 42. Pickering, B.S., Neely III, R.R., Harrison, D., 2019. The Disdrometer Verification Network (DiVeN):
668 a UK network of laser precipitation instruments. *Atmospheric Meas. Tech.* 12, 5845–5861.
669 <https://doi.org/10.5194/amt-12-5845-2019>
- 670 43. Qin, S., Wang, K., Wu, G., Ma, Z., 2021. Variability of hourly precipitation during the warm season
671 over eastern China using gauge observations and ERA5. *Atmospheric Res.* 264, 105872.
672 <https://doi.org/10.1016/j.atmosres.2021.105872>
- 673 44. Randel, D.L., Kummerow, C.D., Ringerud, S., 2020. The Goddard Profiling (GPROF) Precipitation
674 Retrieval Algorithm, in: Levizzani, V., Kidd, C., Kirschbaum, D.B., Kummerow, C.D., Nakamura, K.,

- 675 Turk, F.J. (Eds.), *Satellite Precipitation Measurement: Volume 1, Advances in Global Change Research*.
676 Springer International Publishing, Cham, pp. 141–152. https://doi.org/10.1007/978-3-030-24568-9_8
- 677 45. Renard, K.G., 1997. *Predicting Soil Erosion by Water: A Guide to Conservation Planning with the*
678 *Revised Universal Soil Loss Equation (RUSLE)*. U.S. Department of Agriculture, Agricultural
679 Research Service.
- 680 46. Rosewell, C.J., 1986. Rainfall kinetic energy in eastern Australia. *J. Clim. Appl. Meteorol.* 25, 1695–
681 1701. [https://doi.org/10.1175/1520-0450\(1986\)025<1695:RKEIEA>2.0.CO;2](https://doi.org/10.1175/1520-0450(1986)025<1695:RKEIEA>2.0.CO;2)
- 682 47. Sanchez-Moreno, J.F., Mannaerts, C.M., Jetten, V., Löffler-Mang, M., 2012. Rainfall kinetic energy–
683 intensity and rainfall momentum–intensity relationships for Cape Verde. *J. Hydrol.* 454–455, 131–140.
684 <https://doi.org/10.1016/j.jhydrol.2012.06.007>
- 685 48. Sempere-Torres, D., Porrà, J.M., Creutin, J.-D., 1998. Experimental evidence of a general description
686 for raindrop size distribution properties. *J. Geophys. Res. Atmospheres* 103, 1785–1797.
687 <https://doi.org/10.1029/97JD02065>
- 688 49. Sharifi, E., Saghafian, B., Steinacker, R., 2019. Downscaling Satellite Precipitation Estimates With
689 Multiple Linear Regression, Artificial Neural Networks, and Spline Interpolation Techniques. *J.*
690 *Geophys. Res. Atmospheres* 124, 789–805. <https://doi.org/10.1029/2018JD028795>
- 691 50. Tang, G., Clark, M.P., Papalexiou, S.M., Ma, Z., Hong, Y., 2020. Have satellite precipitation products
692 improved over last two decades? A comprehensive comparison of GPM IMERG with nine satellite and
693 reanalysis datasets. *Remote Sens. Environ.* 240, 111697. <https://doi.org/10.1016/j.rse.2020.111697>
- 694 51. Ulbrich, C.W., 1983. Natural Variations in the Analytical Form of the Raindrop Size Distribution. *J.*
695 *Clim. Appl. Meteorol.* 22, 1764–1775.
- 696 52. USDA-Agricultural Research Service, 2013. *RUSLE2 Science Documentation*. Washington, D.C.

- 697 53. van Dijk, A.I.J.M., Bruijnzeel, L.A., Rosewell, C.J., 2002. Rainfall intensity–kinetic energy
698 relationships: a critical literature appraisal. *J. Hydrol.* 261, 1–23. <https://doi.org/10.1016/S0022->
699 1694(02)00020-3
- 700 54. Wischmeier, W.H., Smith, D.D., 1978. Predicting rainfall erosion losses: a guide to conservation
701 planning. Department of Agriculture, Science and Education Administration, United States.
- 702 55. Wischmeier, W.H., Smith, D.D., 1958. Rainfall energy and its relationship to soil loss. *Eos Trans. Am.*
703 *Geophys. Union* 39, 285–291. <https://doi.org/10.1029/TR039i002p00285>
- 704 56. Xie, Y., Yin, S., Liu, B., Nearing, M.A., Zhao, Y., 2016. Models for estimating daily rainfall erosivity
705 in China. *J. Hydrol.* 535, 547–558. <https://doi.org/10.1016/j.jhydrol.2016.02.020>
- 706 57. Xu, S., Shen, Y., Niu, Z., 2019. Evaluation of the IMERG version 05B precipitation product and
707 comparison with IMERG version 04A over mainland China at hourly and daily scales. *Adv. Space Res.*
708 63, 2387–2398. <https://doi.org/10.1016/j.asr.2019.01.014>
- 709 58. Yang, Q., Dai, Q., Han, D., Chen, Y., Zhang, S., 2019. Sensitivity analysis of raindrop size distribution
710 parameterizations in WRF rainfall simulation. *Atmospheric Res.* 228, 1–13.
711 <https://doi.org/10.1016/j.atmosres.2019.05.019>
- 712 59. Yang, Q., Dai, Q., Zhang, S., Zhu, K., Zhang, L. (2022). Raindrop size distribution retrieval model for
713 X-band dual-polarization radar in China incorporating various climatic and geographical elements.
714 *IEEE T. Geosci. Remote.* 60, 1-17.
- 715 60. Yin, S., Xie, Y., Nearing, M.A., Wang, C., 2007. Estimation of rainfall erosivity using 5- to 60-minute
716 fixed-interval rainfall data from China. *CATENA* 70, 306–312.
717 <https://doi.org/10.1016/j.catena.2006.10.011>
- 718 61. Zhu, J., Zhang, S., Yang, Q., Shen, Q., Zhuo, L., Dai, Q., 2021. Comparison of rainfall microphysics

719 characteristics derived by numerical weather prediction modelling and dual-frequency precipitation
720 radar. Meteorol. Appl. 28, e2000. <https://doi.org/10.1002/met.2000>